Nuclear Science and Techniques (2026) 37:50
https://doi.org/10.1007/s41365-025-01869-z

Mitigating emittance and longitudinal profile degradation of non-ideal bunches caused by CSR in multi-bend deflecting beamlines

Xiu-Ji Chen[1,2] · Si Chen[3] · Hai-Xiao Deng[3] · Dong Wang[1,3]

Received: 23 November 2024 / Revised: 21 April 2025 / Accepted: 22 April 2025 / Published online: 10 January 2026

Abstract
Preserving beam quality during the transport of high-brightness electron bunches is crucial for advanced accelerator applications, such as particle colliders, free-electron lasers, and recirculating linacs. However, coherent synchrotron radiation (CSR) significantly degrades beam quality when electron bunches pass through multi-bend isochronous beamlines, particularly for short bunches with non-ideal longitudinal profiles. Although several methods have been proposed to mitigate CSR effects, most rely on small-angle approximations or are limited to idealized bunch profiles. In this study, we present two improved methods for designing isochronous triple-bend achromat (TBA) beamlines that effectively mitigate CSR-induced emittance growth and longitudinal profile distortion without relying on small-angle approximations. The first method, an enhanced integral optimization approach, simplifies numerical optimization and can accurately handle larger deflection angles, making it suitable for practical applications that require flexible lattice configurations. The second method, an optimized *I*-matrix approach, completely cancels steady-state and transient CSR kicks through specific matrix constraints and higher-order dispersion optimization, enabling effective CSR suppression even with very large deflection angles. Systematic simulations demonstrate that both methods achieve excellent preservation of transverse emittance and longitudinal profiles.

Keywords Lattice design · Coherent synchrotron radiation · Horizontal emittance

1 Introduction

Large-angle deflection of high-current, ultra-short electron bunches is essential for achieving higher luminosity and enhanced photon brightness in recirculating linacs and X-ray free-electron lasers [1–7]. However, maintaining bunch quality during deflection is of paramount importance. Coherent synchrotron radiation (CSR) during deflection can severely degrade bunch quality, especially when charged particles traverse a curved trajectory. In this process, the bunch emits coherent radiation that interacts with the constituent particles, significantly impacting their dynamics and, as a result, affecting overall beam quality and performance.

When a relativistic bunch traverses a dipole magnet, CSR is generated if the bunch length is comparable to the radiation wavelength. This radiation induces energy modulation between the bunch head and tail, resulting in distortion of the longitudinal phase space. Additionally, the coupling between transverse and longitudinal directions can lead to degradation of transverse bunch quality [8, 9].

This work was supported by the Natural Science Foundation of Shanghai (No. 22ZR1470200), National Natural Science Foundation of China (Nos. 12125508, 12122514, 12541503, and 12241501), Shanghai Pilot Program for Basic Research—Chinese Academy of Sciences, Shanghai Branch (JCYJ-SHFY-2021-010).

✉ Si Chen
chens@sari.ac.cn

✉ Hai-Xiao Deng
denghx@sari.ac.cn

[1] ShanghaiTech University, Shanghai 201210, China

[2] Shanghai Institute of Applied Physics, Chinese Academy of Sciences, Shanghai 201800, China

[3] Shanghai Advanced Research Institute, Chinese Academy of Sciences, Shanghai 201210, China

Methods for suppressing the CSR effect in compressed multi-bend structures have been extensively studied. The research focuses on achieving both CSR suppression and bunch length compression in compressors [10–16]. Unlike the optimization objective of the compressor, non-compressed multi-bend structures need to maintain the longitudinal profile of bunches while suppressing the CSR effect. Since non-compressed multi-bend structures are often used to bend high-intensity bunches, the intensity of the CSR effect in the isochronous arc region, under the same bending angle, is greater than in the compressor. This can lead to degradation of bunch length, micro-bunching structure, and other properties [17–20].

The triple-bend achromat (TBA) is a relatively simple structure that can adjust the R_{56}, and it is commonly used for beam transport and deflection where preservation of the longitudinal profile is required. Research has also shown that, under certain special designs, the TBA structure can deflect high-brightness bunches while suppressing the CSR effect. The beam envelope matching method minimizes projected emittance growth through Twiss function adjustment, while the *R*-matrix method analyzes CSR effects in achromatic cells and aligns the undisturbed beam distribution in the transverse phase space [21, 22]. The *R*-matrix method was modified in [23] with the objective of analyzing the horizontal displacement caused by CSR in one dipole magnet, which is called the kick-point method. The C-S formalism analysis [11] was also modified and combined with the kick-point method to effectively reduce the transverse emittance growth caused by the CSR effect. Using the kick-point method, Huang derived the general conditions for eliminating CSR effects in a single TBA cell and obtained a set of numerical solutions that could be applied in TBA design [24–26]. Another set of numerical solutions was demonstrated [27, 28], which not only suppressed CSR effects but also achieved optical stability, enabling the serial connection of multiple cells to increase the deflection angle. Moreover, longitudinal control such as R_{56} and T_{566} was applied to maintain the longitudinal profile of the bunch after a 60° deflection, effectively suppressing the gain of microbunching instability (MBI). The integral method achieves CSR suppression through minimizing the integrated $R_{i6}^{s\to s_\mathrm{f}}$ $(i=1,2)$ under small angle approximation in TBA cells [29].

In this study, two methods were employed to optimize a beamline for large-angle deflection to mitigate the effects of CSR. The first method builds on the work in [29, 30]. Our enhanced integral optimization method eliminates the small-angle approximation, enabling accurate CSR suppression even at larger deflection angles. This approach significantly simplifies numerical optimization processes and extends its applicability to various complex lattice designs. The second approach, our optimized *I*-matrix method, systematically cancels both steady-state (ss CSR) and transient CSR (tr CSR) kicks through precise matrix conditions and second-order dispersion optimization. The beamline based on this method effectively suppresses residual CSR kicks and preserves beam quality even after multiple deflection cells, making it particularly suitable for large-angle deflection beamlines. In Sect. 2, the physics model of emittance degradation caused by CSR is introduced, and we further simplify the integral method. In Sect. 3, a single TBA cell is studied to meet multiple requirements, and a multi-objective optimization algorithm (MOGA) is combined with the integral method to design an isochronous TBA structure. In Sect. 4, the *I*-matrix method is used to design a double TBA cell, with further optimizations enabling the bunch to be deflected at a larger angle. Additionally, a brief discussion of the SXFEL upgrade plan and preliminary experimental results is provided. Section 5 concludes the study.

2 Theory analysis for emittance degradation caused by CSR

The effect of CSR on bunches is often investigated using a 1D projected model that neglects vertical influences and considers only longitudinal interactions. Within this approximation, the CSR effect depends exclusively on the natural coordinates s and the longitudinal coordinate of particle z. As the particles are deflected in a beam transport line, the transverse displacements x and x' of the observation point s_f along the beam line can be expressed as:

$$\begin{aligned}\hat{x}(s_\mathrm{f},z) &= \hat{x}_{\beta\&\eta}(s_\mathrm{f},z)+\hat{x}_{\mathrm{csr}}(s_\mathrm{f},z),\\ \hat{x}'(s_\mathrm{f},z) &= \hat{x}'_{\beta\&\eta}(s_\mathrm{f},z)+\hat{x}'_{\mathrm{csr}}(s_\mathrm{f},z),\end{aligned} \tag{1}$$

where $\hat{x}_{\beta\&\eta}$ and $\hat{x}'_{\beta\&\eta}$ are the oscillation motions of the particles constrained by the magnetic elements and are solely dependent on the initial coordinates of the particles in the six-dimensional phase space and lattice parameters. The transverse offsets x_{csr} and x'_{csr} arise due to the coupling between the longitudinal and transverse directions, caused by the energy spread generated by the CSR effect; the energy spread induced by the CSR effect is represented by δ_{csr}, at any point s_i, the variation in energy spread is denoted as $\Delta\delta_{\mathrm{csr},i}$. In the beamline with nonzero dispersion, the coupling terms between the transverse and longitudinal directions lead to additional transverse offsets $\Delta x_{\mathrm{csr},i}$ and $\Delta x'_{\mathrm{csr},i}$, which are produced by $\Delta\delta_{\mathrm{csr},i}$ generated at point s_i. The transverse offsets $\Delta x_{\mathrm{csr},i}$ and $\Delta x'_{\mathrm{csr},i}$ generated at observation point s_f are:

$$\begin{aligned}\Delta x_{\mathrm{csr},i} &= \Delta\delta_{\mathrm{csr},i}R_{16}^{s_i\to s_\mathrm{f}},\\ \Delta x'_{\mathrm{csr},i} &= \Delta\delta_{\mathrm{csr},i}R_{26}^{s_i\to s_\mathrm{f}},\end{aligned} \tag{2}$$

$R_{i6}^{s_i\to s_\mathrm{f}}$ $(i=1,2)$ represents elements R_{16} and R_{26} in the transfer matrix from any point s_i to observation point s_f. The total transverse offset generated by the CSR effect from the initial

point s_0 to the observation point s_f is obtained by summing the transverse offsets $\Delta x_{csr,i}$ and $\Delta x'_{csr,i}$ produced at each point along the path. This sum can be represented in the form of an integral, given as

$$\begin{aligned}\hat{x}_{csr}(z) &= \int_{s_0}^{s_f} \frac{d\delta_{csr}(z)}{ds} \cdot R_{16}^{s\to s_f} ds,\\ \hat{x}'_{csr}(z) &= \int_{s_0}^{s_f} \frac{d\delta_{csr}(z)}{ds} \cdot R_{26}^{s\to s_f} ds.\end{aligned} \tag{3}$$

We define $\hat{x}_{csr}(z)$ and $\hat{x}'_{csr}(z)$ as the CSR kick at point z in the particle longitudinal coordinate. According to the discussion in Sect. A, the CSR-induced energy spread variance for arbitrary longitudinal profiles can be approximated as:

$$\frac{\delta_{csr}}{ds}(u,s) = \frac{k_{csr}}{\sigma_z^{4/3}(s)}\Gamma(u), \tag{4}$$

$\sigma_z(s)$ is the RMS bunch length at point s, $u = \frac{z}{\sigma_z}$ is the normalized longitudinal position, $k_{csr} = \frac{2r_e}{3^{4/3}\rho^{2/3}\gamma}$ and the formula of $\Gamma(u)$ is presented in Eq. (A.2), which is only dependent on the longitudinal profile of the bunches. In this study, we aim to deflect a beam with high peak current while maintaining the distribution of the longitudinal profile. Therefore, two conditions must be satisfied: (i) the lattice must be isochronous, and (ii) the deflection angle of a single bend must be kept small to prevent excessive local effects R_{56}. Larger local R_{56} can cause significant changes in the longitudinal profile of the bunch, potentially leading to irreversible beam degradation. Once the above two conditions are satisfied, the variance in bunch length can be neglected in all regions of the beamline. From Eq. (B.6) in Sect. B, the emittance at the exit of the beamline is

$$\begin{aligned}\varepsilon_x^2 &= \varepsilon_{x0}^2 + \varepsilon_{x0}\left(\beta_{xf}I_1^2 + 2\alpha_{xf}I_1I_2 + \gamma_{xf}I_2^2\right)I_{csr} + \Delta\varepsilon_{csr}^2\\ &= \varepsilon_{x0}^2 + \varepsilon_{x0}\varepsilon_{csr}I_{csr} + \Delta\varepsilon_{csr}^2,\end{aligned} \tag{5}$$

ε_x, ε_{x_0} denote the geometric emittance at the entrance and exit of the beamline, respectively; β_x, α_x, and γ_x are the Twiss functions at the exit of the lattice. The definition of I_i and I_{csr} can be found in Sect. B. when the effects of ss CSR are neglected; $\Delta\varepsilon_{csr}^2 = \langle\Delta x^2\rangle\langle\Delta x'^2\rangle - \langle\Delta x\Delta x'\rangle^2$, when only ss CSR is considered. Therefore, the emittance growth stems from ε_{csr} in Eq. (5). Minimizing this term can suppress the emittance variation induced by ss CSR in the design process. Moreover, for the lattice with periodic solutions, the ε_{csr} can be further simplified to

$$\varepsilon_{csr} = \beta_{x,ps}I_1^2 + I_2^2/\beta_{x,ps}, \tag{6}$$

$\beta_{x,ps} = \sqrt{\hat{M}_{12}^2/(1-\hat{M}_{11}^2)}$ is the periodic solution of TBA cell. Consequently, in this study, an objective function for the lattice with solutions can be defined for evaluating the impact of ss CSR:

$$f_{obj} = \left(\sqrt{\hat{M}_{12}^2/(1-\hat{M}_{11}^2)}I_1^2 + I_2^2/\sqrt{\hat{M}_{12}^2/(1-\hat{M}_{11}^2)}\right). \tag{7}$$

By optimizing the transfer matrix elements as shown in Eq. (7), the integral can be effectively minimized, thereby mitigating the impact of ss CSR. This result is valid for any bunch distribution. The computation of the integral can be achieved either by fitting the evolution of $R_{5i}(i=1,2)$ within the bends during the optimization process or by uniformly sampling points along the bends and summing their contributions. In practical applications, particularly for an asymmetric lattice without periodic solutions, a more universally applicable approach involves deriving all elements of the matrix $\hat{M}$ or adjusting the Twiss functions at the exit of the beamlines as variables to search for the optimal solution.

3 CSR effects in single isochronous TBA cells with periodic optics function

In this study, we focused on the isochronous TBA cells. And the following conditions need to be met to completely eliminate the ss CSR kick in a single TBA cell: (1) and (2): isochronous and achromatic, (3) and (4) I_1 and I_2 equal to zero, (5) $|\hat{M}_{11}+\hat{M}_{22}|<2$. In the case of symmetric TBA configurations with three identical bends, no structure can simultaneously satisfy all the specified conditions [27, 29]. This is due to the fact that the number of constraints exceeds the number of degrees of freedom. As a result, the ratio between the middle bend and the side bends in the symmetric TBA structure is introduced as an additional degree of freedom. An analytical investigation incorporating this additional degree of freedom is presented in Sect. C. In this investigation, it is described that the value of $|\hat{M}_{11}+\hat{M}_{22}|$ decreases with the reduction of the absolute value of the ratio k when conditions (1) to (4) are met; however, its minimum value still reaches $17\frac{1}{4}$. Section C revealed the absence of an exact solution that satisfies all of these conditions, necessitating the search for an asymptotic solution for the symmetric TBA. The Non-dominated Sorting Genetic Algorithm II (NSGA2) [31], a versatile multi-objective optimization algorithm, was employed for this task. It utilizes non-dominated sorting and genetic operators to efficiently generate diverse and effective solutions in a single run. The accelerator physics simulation program BMAD [32] was used to simulate beam dynamics with CSR effects, and to ensure accuracy, the simulation outcomes were validated using the accelerator physics program ELEGANT [33]. All results presented in this paper are based on BMAD simulations and have undergone comparative validation. The parameters of the bunch used in the

simulation are listed in Table 1. The bunch in the first column of the table is a Gaussian bunch with a peak current of 2000 A. The second column represents the actual case, with the non-ideal bunch coming from the Shanghai Soft X-ray Free-Electron Laser (SXFEL) [34, 35], the first X-ray FEL facility in China. Within the TBA design, the angular ratio between the middle bend and the side bends is defined as k, resulting in a total deflection angle of 15°. The TBA assembly comprises six quadrupole magnets and four sextupole magnets, intricately arranged to refine both the first- and second-order transfer matrices. The strategic placement and calibrated strengths of these magnets exhibit a symmetrical distribution with respect to the central axis of the TBA cell.

The asymptotic solution must lie within the optically stable region of the isochronous TBA structure. By combining the achromatic, isochronous, and symplectic conditions of the transfer matrix, it is known that for any given k, the two optical stability regions of the isochronous TBA structure are denoted as regions S1 and S2 in Fig. 1. The S1 region is defined within the interval $[-k, -k/2]$, which aligns precisely with the curves in Fig. 13, where $I_1 = 0, S2$ and $I_2 = 0, S2$. Notably, within the S1 region, the magnitudes of I_1 and I_2 are observably lower than those within the S2 region. Furthermore, the ε_{csr} was calculated within the S1 region which is defined in Eq. (6). When m_{22} approaches $-k$ or $-k/2$, as shown in Fig. 2, ε_{csr} becomes smaller than in other cases in region S1, resulting in a lesser impact of ss CSR on the transverse quality of the bunch. It is worth mentioning that the TBA

Table 1 Bunch parameter of simulation

Parameters	Gaussian bunch	SXFEL bunch
Bunch length (μm)	30	57
Beam energy (MeV)	1500	1500
Normalized emittance (μm rad)	1	1.19
Bunch charge (pC)	500	500
Relative rms energy spread (%)	0.05	0.06

Fig. 1 (Color online) Optical stability region for a symmetric isochronous TBA structure

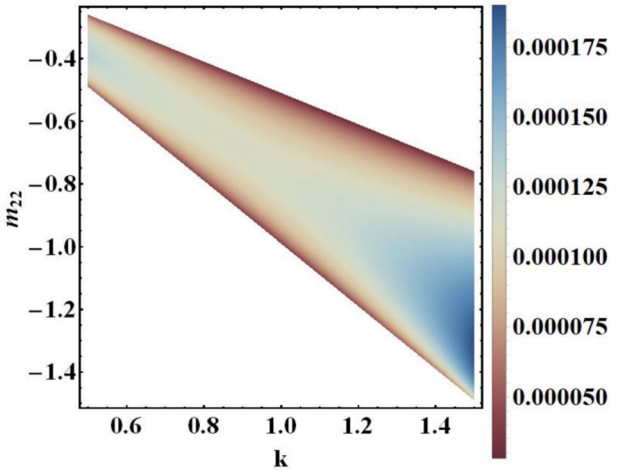

Fig. 2 (Color online) ε_{csr} in S1, the two boundaries of this region are, respectively $m_{22} = -k/2$ and $m_{22} = -k$

structures corresponding to $m_{22} = -k$ and $m_{22} = -k/2$ have $\hat{M}_{11} = \hat{M}_{22} = 1$ with a nonzero $\hat{M}_{12}$, which indicates that these TBA cells do not have a periodic solution for the β function. Simultaneously, the periodic solutions corresponding to the β function are large in the adjacent areas of $m_{22} = -k$ and $m_{22} = -k/2$, although theoretical calculations indicate that the ss CSR does not have a significant impact in these cases. Therefore, when considering the impact of TR CSR at the entrance and exit of the bend, x_{csr} and x'_{csr} no longer conform to the form described in Sect. B. Furthermore, when $m_{22} = -k$ or $m_{22} = -k/2$, $\langle x^2_{csr} \rangle$ or $\langle x'^2_{csr} \rangle$ no longer equals zero. As known from Eq. (5), a larger β_x and γ_x coupled with the residuals $\langle x'^2_{csr} \rangle$ and $\langle x^2_{csr} \rangle$ will lead to a significant increase in emittance. Therefore, in the optimization process of this study, the β function corresponding to the periodic solution was constrained to lie within the range [0.5, 1.5] to effectively mitigate this effect.

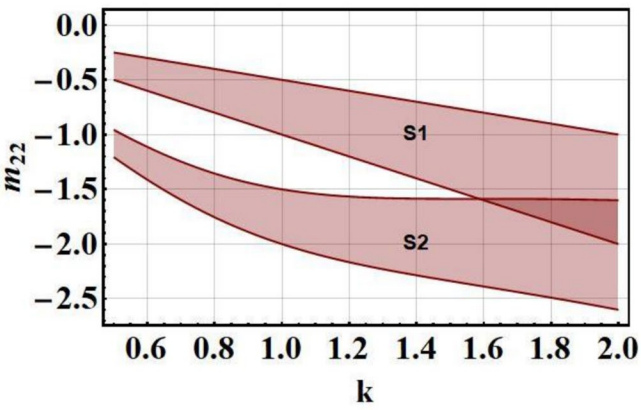

In the optimization process, a set of 12 variables is used. These include three quadrupole magnet strengths (ranging from $[-10, 10]$), two sextupole magnet strengths (ranging from $[-500, 500]$), one angular ratio k (between the middle and side bends (ranging from [0.2, 2]), and six drift lengths between magnetic elements (each ranging from [0.1, 2]). The optimization is formulated as a multi-objective problem with two goals:

$$f_{\text{obj1}} = f \times \left(\sqrt{\hat{M}_{12}^2/(1-\hat{M}_{11}^2)} I_1^2 + I_2^2 / \sqrt{\hat{M}_{12}^2/(1-\hat{M}_{11}^2)} \right),$$
$$f_{\text{obj2}} = f \times \left| (R_{56} \times \delta_{\text{e}} + T_{566} \times \delta_{\text{e}}^2)/\sigma_z \right|, \tag{8}$$

where f_{obj1} represents the impact of the ss CSR on the transverse dimension. As discussed in Sect. 2, it denotes the minimum growth in emittance when $\alpha_x = 0$ at the exit of the TBA. f_{obj2} denotes the relative change in bunch length due to passage through the TBA while accounting for second-order effects. f is an additional coefficient that equals 1 when the TBA satisfies the following conditions: (1) $\hat{M}_{26,\text{mid}} < 10^{-4}$; (2) $\left|\hat{M}_{ii} + \hat{M}_{jj}\right| \leq 2 \quad (i = 1, 3; j = 2, 4)$ (3) $0.5 \leq \sqrt{\hat{M}_{12}^2/(1-\hat{M}_{11}^2)} \leq 1.5$; otherwise, it is a large number related to these conditions. Condition (1) ensures that the TBA structure is achromatic. Conditions (2) and (3), on the other hand, are designed to enforce the existence of a periodic solution in the TBA cell, characterized by low values of the β and γ functions. The value of I_1 and I_2 within f_{obj1} was calculated by uniformly distributing points across the lattice. The parameter n is the number of points in TBA cell. When $n = 1000$, the error between the statistical result and the actual result is within 5%. It is worth mentioning that when I_i is significantly smaller than the maximum value of R_{5i} of the lattice, then this method may lose accuracy. The results can be made more precise by either increasing the number of points or employing curve fitting method. After evolving over 500 generations, the optimization results converged. Figure 3 illustrates the objective functions and key parameters of the TBA in the final generation. As shown in Fig. 3a, the solutions converge toward a working point near $m_{22} \approx -k/2$ (the dashed line in the figure), which is consistent with the results in Fig. 2. However, due to errors introduced by the small-angle approximation and constraints imposed by the periodic conditions of the beta functions, the solutions do not converge indefinitely toward this boundary. Then, two notable cases are marked: case A ($f_{\text{obj1}} = 3 \times 10^{-5}, f_{\text{obj2}} = 2 \times 10^{-5}$) and case B ($f_{\text{obj1}} = 2 \times 10^{-5}, f_{\text{obj2}} = 0.01$), which correspond to the emphasis on preserving the longitudinal profile and suppressing the emittance growth caused by the ss CSR effects, respectively.

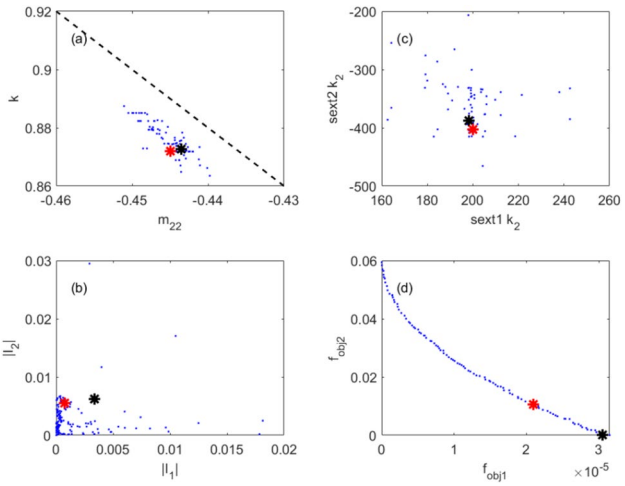

Fig. 3 (Color online) Distribution of solutions in the final generation. **a** Relationship between the bending ratio k and the transfer matrix element m_{22} as defined in Eq. (C.2). **b** Values of $|I_1|$ and $|I_2|$ computed without the small-angle approximation. **c** Sextupole strengths k_2 for the two sextupoles in the TBA cell. **d** Pareto front illustrating the two objective functions. Red and black asterisks denote the selected solutions corresponding to Case A and Case B

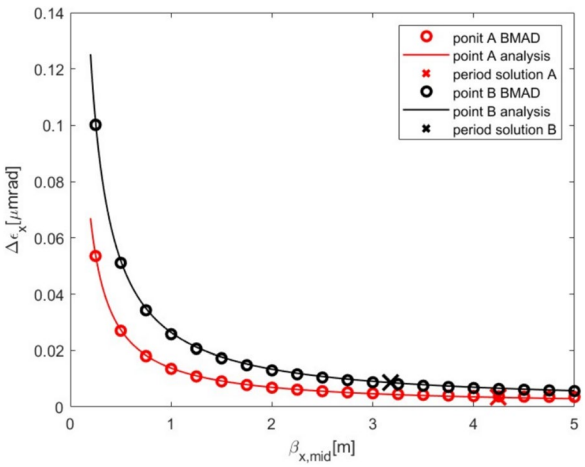

Fig. 4 (Color online) For both TBA cases, the emittance growth induced by ss CSR is illustrated: the solid curve represents the theoretical analysis, the circular markers (o-markers) denote the simulation results obtained using BMAD, and the cross markers (x-markers) correspond to the cases where the optics satisfy the periodic solution

To thoroughly evaluate the suppression capability of ss CSR in Case A (point A) and Case B (point B), we altered the beta function at the midpoint of the TBA under the condition $\alpha_{x,\text{mid}} = 0$ and employed the transfer matrix from the midpoint to the endpoint in conjunction with Eq. (5) to theoretically predict the emittance variation at the TBA exit under symmetric optical conditions (as shown by the curve in Fig. 4). Simulation results across different $\beta_{x,\text{mid}}$ values reveal that a larger β function leads to more gradual emittance growth, consistent

with theoretical predictions, as indicated by the circular markers in Fig. 4. Furthermore, for practical implementation involving the serial connection of multiple TBA cells, the periodic solution—denoted by the cross markers in Fig. 4—deserves special attention. When using a Gaussian bunch as specified in Table 1, the emittance growth due to ss CSR in both Case A and Case B remains below 1%. However, the bunch length variation in Case B is only 16% of that observed in Case A. For the transport of high peak current beams, preserving the longitudinal beam profile is as critical as minimizing emittance growth. Therefore, Case B is selected to ensure both the transverse and longitudinal beam qualities are well maintained across multiple connected TBA cells.

In the simulation work, to better reflect realistic beam dynamics, the effects of TR CSR from components upstream and downstream of the bend were also taken into account. The default order of magnetic elements was set to three. Simulation results for a single TBA cell are summarized in Table 2. As the bunch propagates through a TBA cell, the variation in bunch length for both bunch profiles remains below 0.1%. When only ss CSR is considered, the emittance growth is limited to less than 1%, which is in good agreement with the theoretical predictions from Eq. (5). However, when TR CSR is included, the emittance increases by approximately 3% compared to simulations neglecting CSR effects.

In the simulation of the multi-cell TBA structure, six TBA cells were connected in series to achieve a total deflection angle of 90°. In this section, the values of I_1 and I_2 at the exit of each cell were computed and compared with the results from ss CSR simulations. In the multi-cell configuration, emittance variation is influenced not only by $I_{1,2}$, but also by the transfer matrix of each individual TBA cell, as I_1 and I_2 are not exactly zero. Consequently, their values differ at the exits of various cells. To determine these values, the R_{51} and R_{52} curves were extracted from BMAD for the cascaded cell configuration. Furthermore, to maintain statistical accuracy, the number of sampling points was scaled proportionally to the number of connected TBA cells. For example, when calculating I_1 and I_2 at the exit of the sixth TBA cell, the *curve_n_pts* parameter was set to 6000. As illustrated in the top panel of Fig. 5, the theoretical analysis based on Eq. (5) aligns well with the simulation results for the multi-cell TBA scenario. When including both ss CSR and TR CSR effects, the emittance growth for both bunch types is presented in Fig. 5. Simultaneously, the bunch length was well preserved throughout the structure, as

Table 2 Simulation result of single TBA cell in BMAD

Parameters	$\frac{\Delta\sigma_z}{\sigma_z}$ (%)	$\frac{\Delta\epsilon_{ss}}{\epsilon_0}$ (%)	$\frac{\Delta\epsilon_{tr+ss}}{\epsilon_0}$ (%)
Gaussian bunch	0	0.87	2.6
SXFEL bunch	0.02	0.83	3.4

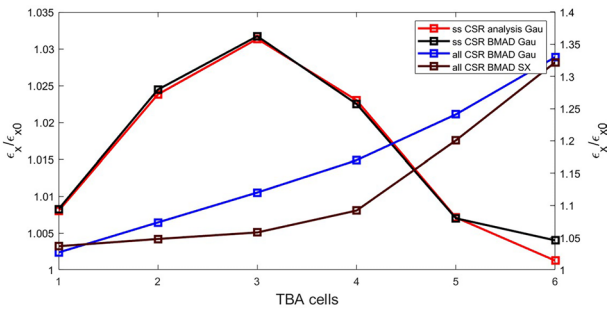

Fig. 5 (Color online) Simulation results of multi-cell TBA cells in BMAD: (top) emittance growth. 'Gau' represents the Gaussian bunch, and 'SX' represents the SXFEL bunch. The left *Y*-axis represents the case considering only ss CSR, and the right *Y*-axis represents the case considering ss CSR and tr CSR

depicted in Fig. 6, with less than 1% variation observed for both bunch profiles.

For the Gaussian bunch, the longitudinal profile remained well-preserved throughout the bunch range. At the exit of the sixth TBA cell, there was no significant deviation from the initial bunch profile, as shown by the red and black lines in the right panel of Fig. 6. For the SXFEL bunch, the longitudinal profile in the core region (highlighted within the purple box in the left panel of Fig. 6) was well-maintained. However, degradation in bunch quality was primarily observed at the sides of the bunch. As indicated by the black curve in the left image of Fig. 6, the slices at the edges of the bunch exhibited higher current intensity and steeper gradients in current strength. In practical applications, the core region of the bunch is typically of primary interest. Therefore, the impact of CSR effects on the longitudinal profile of the bunch can be considered negligible within a limited number of cells. For small-angle deflections, the single TBA structure used in this study effectively mitigates beam quality degradation. Compared to the two-cell configuration discussed in Sect. D, the single TBA cell is more practical due

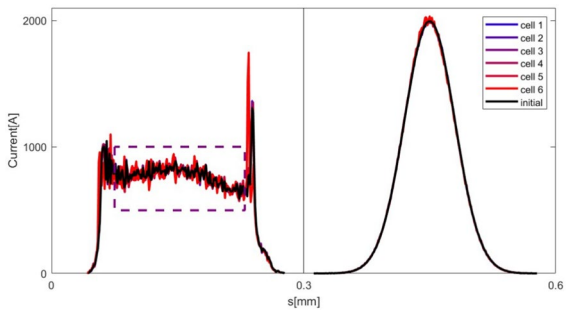

Fig. 6 (Color online) The longitudinal profile of the bunch at the exit of each TBA cell. (Left) The SXFEL bunch; (Right) The Gaussian bunch. The black line represents the initial bunch and the term 'cell *i*' refers to the bunch located at the exit of the *i*th TBA cell. The purple box with dash line is the core region of SXFEL

to its simpler structure and fewer magnets. However, as the number of cells increased, the projected emittance exhibited a noticeable rise for both bunch types. This increase can be attributed to the neglected CSR effects during the sequence drift and at the entrance of the bends in the design phase. Previous studies have shown that completely canceling CSR effects in the sequence drift of TBA cells is impossible [36].

4 CSR effects in double isochronous TBA cells with periodic optics function

For a single isochronous TBA cell, the complete elimination of ss CSR effects remains a challenge. As outlined in Sect. 3, an optimal working point is determined that strikes a balance between suppressing CSR effects and preserving the longitudinal bunch profile. Although the design and optimization process considers only the ss CSR kick, the TBA configuration presented in Sect. 3 proves highly effective in mitigating CSR kick, both in theoretical analysis and simulations. However, as the number of cascaded cells increases, the quality of the bunch progressively degrades. This degradation is primarily due to the cumulative impact of tr CSR effects throughout the beam transport process. Similar to Eq. (5) for ss CSR, the tr CSR kick, in combination with the Twiss functions, contributes to a significant increase in emittance. Consequently, to achieve larger deflection angles while preserving beam quality, it becomes crucial to simultaneously suppress both tr and ss CSR effects.

A $-I$ matrix between bends with identical deflection directions (while an I matrix for bends with opposite deflection directions) is a common approach to suppress ss CSR kicks: For any points s_{A} and s_{B} in bends A and B, the R_{5i} meets

$$R_{5i}(s_{\mathrm{A}}) = -R_{5i}(s_{\mathrm{B}}) \quad (i = 1, 2). \tag{9}$$

This results in the complete cancelation of the ss CSR kick. Following the four cases presented in [37], we investigate the energy spread induced by tr CSR. The analysis assumes constant magnetic fields in the bends and negligible bunch length variation. Under these conditions, the energy spread induced by tr CSR depends on two key parameters: the position s' relative to the entrance of the single n-bend achromatic structure (TBA in this study), and the position x relative to the upstream bend. So, for any s' and x in double TBA cell, δ'_{csr} meets

$$\delta'_{\mathrm{csr,A}}(s', x) = \delta'_{\mathrm{csr,B}}(s', x). \tag{10}$$

The subscript 'A' and 'B' denote any points in different TBA in double TBA cells. Moreover, similar to Eq. (9), the transfer matrix for the reverse beamline (detailed description provided in Sect. B) satisfies:

$$\begin{aligned} R_{5i}(s') &= -R_{5i}(s' + L), \\ R_{5i}(x) &= -R_{5i}(x + L), \end{aligned} \tag{11}$$

L is the distance between the entrances of adjacent TBA cells. Thus, for the beamline consisting of two TBA cells, the reverse beamline meets

$$\begin{aligned} \int_{s_{\mathrm{f}}+L}^{s_0+L} R_{52}(s')\delta'_{\mathrm{csr,B}}(s')\mathrm{d}s' + \int_{s_{\mathrm{f}}}^{s_0} R_{52}(s')\delta'_{\mathrm{csr,A}}(s')\mathrm{d}s' = 0, \\ \int_{s_{\mathrm{f}}+L}^{s_0+L} R_{51}(s')\delta'_{\mathrm{csr,B}}(s')\mathrm{d}s' + \int_{s_{\mathrm{f}}}^{s_0} R_{51}(s')\delta'_{\mathrm{csr,A}}(s')\mathrm{d}s' = 0. \end{aligned} \tag{12}$$

Based on the I matrix method, a large-angle deflection beamline was designed, with a focus on investigating the CSR effects on high-peak-current bunches. A detailed overview of this design is provided in Sect. D. As the bending angles within the TBA cell increase, the local R_{56} becomes more significant, which invalidates the rigid beam approximation. This leads to substantial and unpredictable growth in the CSR kick. To maintain the validity of the rigid beam approximation, the number of TBA cells in series should be increased proportionally with the bending angle. Additionally, when two double TBA cells with a $-I$ matrix are connected in series, inserting an I matrix between them further enhances the suppression of the CSR kick at the exit of the beamline.

Figure 7 illustrates a simple model for CSR kick error cancelation achieved through an I matrix. While the Double TBA cell theoretically suppresses CSR effects, higher-order dispersion and local bunch length variations result in residual nonzero values of x_{csr} and x'_{csr} at the double TBA cells exit. The err_i in Fig. 7 represents the residual values at the i-th double TBA cell. A $-I$ matrix connection between double TBA cells results in aligned err_1 and err_2, leading to cumulative errors with increasing cell numbers (top inset in Fig. 7). In contrast, an I matrix connection generates opposing errors that mutually cancel each other (bottom inset in Fig. 7). These errors result in CSR-induced displacements across different slices, ultimately contributing to emittance growth.

Figure 8 presents the simulation results for both cases, with the bunch parameters provided in Table 1. The I matrix configuration results in smaller displacements, which helps preserve the bunch quality. Conversely, for the double TBA

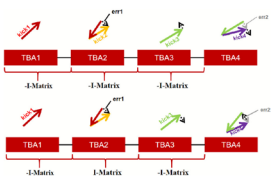

Fig. 7 (Color online) The CSR kick errors can be mutually canceled by introducing an I matrix between double TBA cells with $-I$ matrix

cell described in Sect. D, implementing a $-I$ matrix between two double TBA cells effectively reduces these displacements.

Furthermore, to achieve larger deflection angles while suppressing CSR-induced emittance and maintaining the longitudinal profile, the second-order matrix cannot be neglected. Similar to $R_{i6}^{s\to s_f}$, the second-order matrix element T_{ij6} couples with the additional energy spread, leading to growth in ϵ_i. The elements of the second-order matrix can be expressed as

$$T_{ijk} = g_{jk}\int_0^{s_f} \mathrm{d}s R_{ia}(s\to s_f) B_{abc} R_{bj} R_{ck}, \tag{13}$$

where B_{abc} is the quadratic coefficient of x_b and x_c in the dynamical differential equation for x_a. It depends solely on the type of elements and remains constant for uniform elements. And

$$g_{jk} = \begin{cases} 2 & j \neq k, \\ 1 & j = k. \end{cases} \tag{14}$$

To simplify the formula of Eq. (13), we employ Einstein's summation convention, where repeated indices imply summation, and the summation signs are omitted in Eq. (13). Under the assumption that the matrix between the entrances of two TBA cells is a $-I$ matrix, we have:

$$\begin{cases} R_{jk}(s') = -R_{jk}(s'+L) & j \neq 5,6 \\ R_{jk}(s') = R_{jk}(s'+L) & \text{otherwise}, \end{cases} \tag{15}$$

and

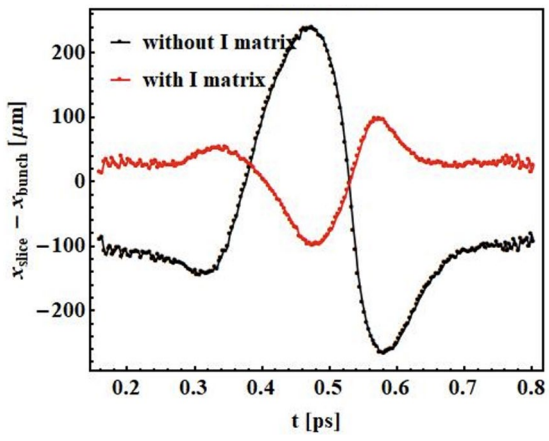

Fig. 8 The CSR-induced displacements along the x-axis at the exit of the second double TBA cell are shown for two configurations: black points represent the case with a $-I$ matrix between the double TBA cells, while red points indicate the case with an I matrix connection. Here, x_{bunch} refers to the center of the entire bunch, and x_{slice} represents the center of each individual slice

$$\begin{cases} R_{ij}^{s\to s_f} = -R_{ij}^{s+L\to s_f}, & j \neq 5,6 \\ R_{ij}^{s\to s_f} = R_{ij}^{s+L\to s_f}, & \text{otherwise}. \end{cases} \tag{16}$$

In this investigation, we focus on a beamline system characterized by horizontal-plane bending and the absence of $x-y$ coupling in its first-order transfer matrix. A significant consequence of Eqs. (15) and (16) is that T_{ijk} vanishes when the indices (i, j, k) contain an even number (including zero) of occurrences of 5 or 6. This mathematical property leads to an important result: the second-order dispersion terms (specifically T_{166} and T_{266}) automatically vanish for the double TBA cell configuration. To effectively control the horizontal emittance growth, four critical second-order matrix elements require careful consideration: T_{116}, T_{126}, T_{216}, and T_{226}. Furthermore, in a symmetric beamline configuration, we observe the relationship $T_{116} = -T_{226}$. For beamlines with either an I or $-I$ transfer matrix, the Twiss functions exhibit periodic behavior under all conditions, with $\alpha = 0$ being characteristic of periodic arc-like sections. The emittance growth at the beamline exit follows a formulation similar to Eq. (6), where β_{ps} can assume arbitrary values. However, the CSR kick must also include higher-order terms. For $\beta_{ps} > 1$, the CSR kick in x' provides the dominant contribution, with its effect strengthening as β_{ps} increases. Conversely, when $\beta_{ps} < 1$, the CSR kick in x dominates and becomes stronger as β_{ps} decreases.

From a practical implementation perspective, extremely small initial β functions impose stringent requirements on upstream focusing conditions. To address this, we adopt $\beta_{ps} > 1$ in the current design work, with particular emphasis on mitigating the CSR kick effects in the x'-axis. While the calculation of $T_{ijk}^{s\to s_f}$ presents significant mathematical challenges, the optimization strategy of minimizing the T_{2j6} terms in the double TBA cell configuration proves effective in reducing the CSR effects from the upstream TBA cell. In the design process, three quadrupoles in the TBA cells are optimized to ensure achromatic and isochronous conditions. Matching sections are added to both sides of the TBA to achieve an overall $-I$ transfer matrix while maintaining $T_{226} = 0$. Two families of sextupoles are then incorporated into the lattice to minimize T_{566} and T_{216}. The beamline consists of six double TBA cells designed to achieve a 180° deflection. Additionally, a matching section between the final two double TBA cells forms an I-matrix for error elimination. Figure 9 illustrates the x'-axis displacements at the beamline exit for both cases with and without T_{216} correction. Relative to the uncorrected case (black dots), reducing $|T_{216}|$ (red dots) effectively controls the displacements, thereby suppressing CSR kicks in the x' axis. This results in reduced growth in horizontal emittance. The simulation results incorporating both tr CSR and ss CSR effects are shown in Figs. 10 and 11, with the initial bunch parameters

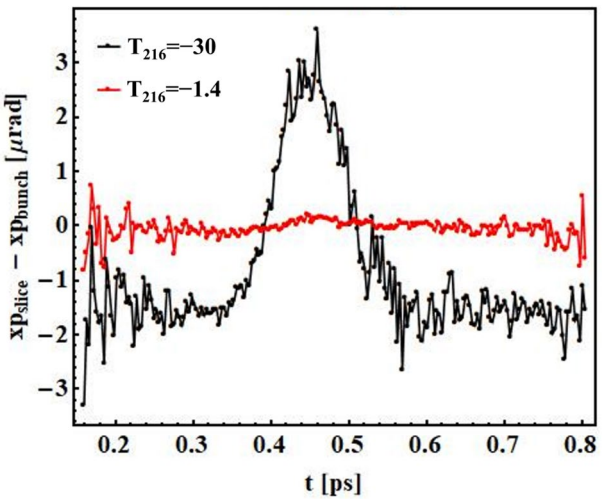

Fig. 9 The CSR-induced displacements along the x'-axis at the beamline exit are shown, where red and black dots represent the cases with and without T_{216} correction

listed in Table 1. Figure 10 shows the projected emittance at the exit of multiple double TBA cells for different bunches. For the Gaussian bunch, although the projected emittance increases with the number of double TBA cells, the growth remains below 25%. Meanwhile, the longitudinal profile and slice emittance of the Gaussian bunch remain nearly unchanged, as shown in the left inset of Fig. 11. The variation in projected emittance is primarily attributed to centroid offsets. For the SXFEL bunch, the emittance growth reaches approximately 35% at the exit of the sixth double TBA cell. As shown in the right inset of Fig. 11, significant variations occur at the bunch edges due to the dramatic changes in current distribution at both the head and tail regions. Moreover, for quasi-uniform bunches, the CSR effect exhibits a stronger influence at the bunch tail, leading to intense CSR effects in these regions and resulting in projected emittance degradation. Similar phenomena are observed in the simulation results for the single TBA cell, as shown in Fig. 6. However, the emittance degradation in the core region (the purple box in Fig. 6) remains negligible, and the projected emittance

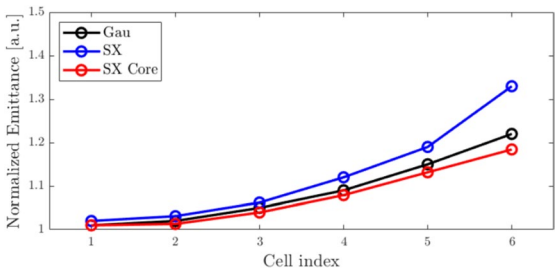

Fig. 10 The normalized project emittance evolution at the exit of multiple double-TBA cells. The 'SX Core' denotes the purple box with dashed line in Fig. 6

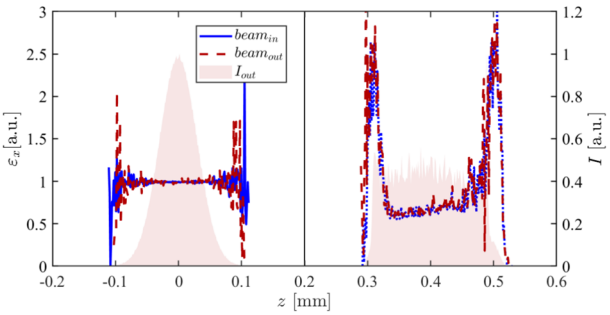

Fig. 11 (Color online) The longitudinal profiles at the exit of the 6th double TBA cell and the normalized slice emittance of the bunches presented in Table 1

growth for this region stays below 20%, which is an acceptable range for the primary radiation region of FELs.

5 Conclusion

This study introduces two enhanced methods for CSR suppression in isochronous structures, addressing the challenges associated with high-peak-current bunch transport through bending systems.

For single TBA cells, the reverse beamline design facilitates an effective evaluation of ss CSR effects without relying on small-angle approximations. This approach preserves excellent transverse beam quality and longitudinal profiles, even under the combined ss and tr CSR effects, proving particularly effective for small bending angles. Furthermore, the reverse beamline optimization method directly determines CSR kicks through accelerator simulations, eliminating the need for additional calculations. This streamlined process not only enhances the efficiency of the design phase but also extends its applicability to more complex structures, such as Multi-Bend Achromats (MBA).

The $-I$ matrix method has been further enhanced through two key improvements: implementing an I matrix between cells and optimizing the higher-order term T_{216} to effectively reduce CSR-induced displacements in the horizontal phase space. This enhanced approach theoretically suppresses both ss and tr CSR effects. For large bending angles, the $-I$ matrix method shows exceptional preservation of bunch quality. Our study demonstrates that combining these improvements allows a configuration of six double TBA cells to achieve a 180-degree deflection while maintaining both transverse emittance and longitudinal profiles for bunches with varying longitudinal distributions. Experimental validation of CSR suppression using the I matrix method is currently underway at SXFEL, with further research planned for future development.

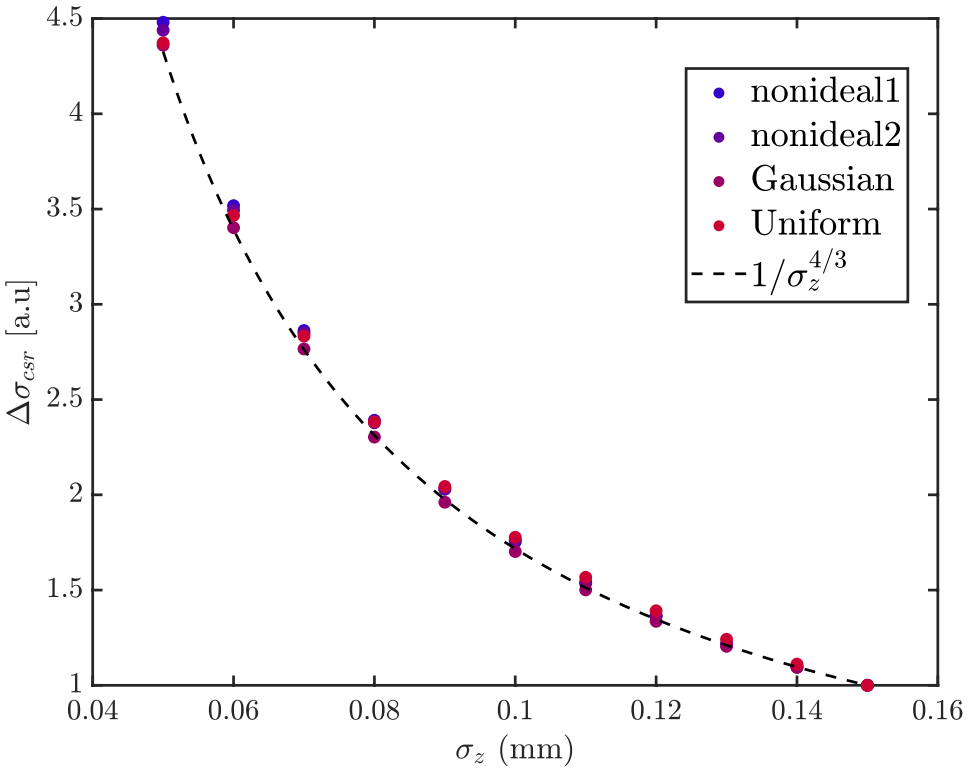

Fig. 12 The simulation of ss CSR for bunches with different longitudinal profiles. The dependence of $\Delta\sigma_{\mathrm{csr}}$ on bunch length maintains consistent characteristics across all bunch longitudinal profiles

Appendix

A. The variance in energy spread caused by steady-state CSR

Assuming that the magnet is uniform, P' is the radiation point, and P is the observation point. ss CSR is considered in this study; other cases are neglected in the subsequent derivations. For an ultra-relativistic beam where $\sigma_z < \rho\phi_{\mathrm{B}}^3/24$ and the bunch density approaches zero near z_{tail} (the position of the tail particle), the ss CSR energy spread can be written as [38]

$$\frac{\mathrm{d}\delta_{\mathrm{csr}}}{\mathrm{d}s}(z) = \frac{2r_{\mathrm{c}}}{3^{4/3}\rho^{2/3}\gamma}\int_{-z_{\mathrm{tail}}}^{z}\frac{1}{(z-z')^{4/3}}\lambda(z')\mathrm{d}z'. \tag{A.1}$$

ρ is the dipole radius, γ is the relativistic factor, r_{c} is the classical radius of the electron, $\lambda(z,s)$ is the normalized longitudinal density of the bunch at point s. Equation (A.1) can be expressed in a more commonly used form following a convolution integral. Furthermore, by substituting z with the normalized longitudinal position $u = \frac{z}{\sigma_z}$, the additional energy spread caused by ss CSR can be expressed as

$$\delta'_{\mathrm{csr}}(u) = \frac{2r_{\mathrm{e}}}{3^{4/3}\rho^{2/3}\gamma\sigma_z^{4/3}}\Gamma(u), \tag{A.2}$$

where

$$\Gamma(u) = \int_{-u_{\mathrm{tail}}}^{u}\frac{1}{(u-u')^{4/3}}\lambda(u')\mathrm{d}u'. \tag{A.3}$$

The $\frac{\mathrm{d}\delta_{\mathrm{csr}}}{\mathrm{d}s}$ in Eq. (A.1) was simplified as δ'_{csr} in Eq. (A.2). Then, Eq. (A.1) consists of two fundamental terms: the $\Gamma(u)$ function that characterizes only the longitudinal distribution shape, independent of other beam parameters, and a scaling factor that accounts for bunch-specific parameters. Based on statistical principles, the u remains invariant under linear transformations. Therefore, for cases where bunches are in isochronous structures or only linear compression is considered in the compressor, the $\Gamma(u)$ remains constant. Thus,

$$\frac{\delta'_{\mathrm{csr}}(u,s_1)}{\delta'_{\mathrm{csr}}(u,s_2)} = \left(\frac{\sigma_z(s_2)}{\sigma_z(s_1)}\right)^{\frac{4}{3}}, \tag{A.4}$$

and

$$\frac{\Delta\sigma_{\mathrm{csr}}(s_1)}{\Delta\sigma_{\mathrm{csr}}(s_2)} = \left(\frac{\sigma_z(s_2)}{\sigma_z(s_1)}\right)^{\frac{4}{3}}. \tag{A.5}$$

The $\Delta\sigma_{\mathrm{csr}}(s) = \left\langle \delta'_{\mathrm{csr}}(u,s)\cdot\Delta s\right\rangle_u$ is the RMS variance in energy spread caused by ss CSR at s. The expression in Eq. (A.1) is not limited to any specific distribution; therefore, the relationship established in Eq. (A.4) and Eq. (A.5) holds true for any bunch distribution, not just for Gaussian bunches. The simulation of ss CSR for bunches with varying longitudinal profiles is illustrated in Fig. 12. The energy spread variance across all four bunch types exhibits a σ_z dependence that conforms to the relationship given in Eq. (A.5), demonstrating that $\Delta\sigma_{\mathrm{csr}}$ follows a universal $1/\sigma^{4/3}$ scaling regardless of the bunch longitudinal distribution.

B. The RMS of the ss CSR kick

According to the discussion in Sect. A and Eqs. (3)–(4), the ss CSR kick at the exit of beamline for any u can be expressed as

$$\begin{aligned}\hat{x}_{\mathrm{csr}}(u) &= k_{\mathrm{csr}}\int_{s_0}^{s_{\mathrm{f}}}\frac{R_{16}^{s\to s_{\mathrm{f}}}}{\sigma_z^{4/3}(s)}\mathrm{d}s\cdot\Gamma(u),\\ \hat{x}'_{\mathrm{csr}}(u) &= k_{\mathrm{csr}}\int_{s_0}^{s_{\mathrm{f}}}\frac{R_{26}^{s\to s_{\mathrm{f}}}}{\sigma_z^{4/3}(s)}\mathrm{d}s\cdot\Gamma(u).\end{aligned} \tag{B.1}$$

To anticipate the influence of ss CSR during the optimization process, we simplify Eq. (B.1). However, in practical design processes, it is common to optimize the transmission matrix with a fixed initial point rather than a fixed endpoint. To find a substitute for $R_{i6}^{s\to s_{\mathrm{f}}}$, we assume that there are only bends, quadrupoles, and drifts in the beamline and that there is no coupling between the horizontal and vertical directions. Due to the properties of the transfer matrix and the symplectic condition:

$$\hat{M}_{s_0}^{s_{\mathrm{f}}}\hat{S}(\hat{M}_{s_0}^{s_{\mathrm{f}}})^{\mathrm{T}} = \hat{S}. \tag{B.2}$$

$\hat{M}_s^{s_{\mathrm{f}}}$ is the transfer matrix from s to s_{f}. $\hat{M}^{\mathrm{T}}$ is the transpose matrix of $\hat{M}$. $\hat{S}$ is the matrix sometimes called the symplectic form which meets $\hat{S}^2 = -I$. And it is easy to derive

$$\left(\hat{M}_s^{s_{\mathrm{f}}}\right)_{16} = \left(\hat{M}_{s_{\mathrm{f}}}^{s}\right)_{52},\quad \left(\hat{M}_s^{s_{\mathrm{f}}}\right)_{26} = -\left(\hat{M}_{s_{\mathrm{f}}}^{s}\right)_{51}. \tag{B.3}$$

The following abbreviations R_{51} and R_{52} are used for $\left(\hat{M}_{s_{\mathrm{f}}}^{s}\right)_{51}$ and $\left(\hat{M}_{s_{\mathrm{f}}}^{s}\right)_{52}$, respectively. The $R_{16}^{s\to s_{\mathrm{f}}}$ and $R_{26}^{s\to s_{\mathrm{f}}}$ appearing in Eq. (B.1) can be substituted with R_{52} and $-R_{51}$, respectively. This substitution necessitates appropriate adjustments to the integration limits. In the optimization process, the exit point of the lattice s_{f} is set as the optimized initial point. This reversed lattice configuration is abbreviated as "reverse beamline" for ease of description in this study. Additionally, during reverse integration, the CSR-induced energy spread must be enforced to remain consistent with the forward integration direction, which corresponds to the actual direction of beam motion. It is important to note that this step is introduced purely for computational convenience and does not have a physical basis. Furthermore, the influence of ss CSR kicks on the overall bunch must be carefully examined to ensure that the optimization process accounts for potential changes in beam quality due to these effects. Specifically, the goal is to analytically determine the values of $\left\langle x_{\mathrm{csr}}^2\right\rangle_u$ and $\left\langle x_{\mathrm{csr}}'^2\right\rangle_u$ at the exit of beamline, where $\langle\rangle_u$ denotes the averaging over the longitudinal distribution in phase space. Based on principles of statistics, the impact of ss CSR on the overall bunch can be expressed as

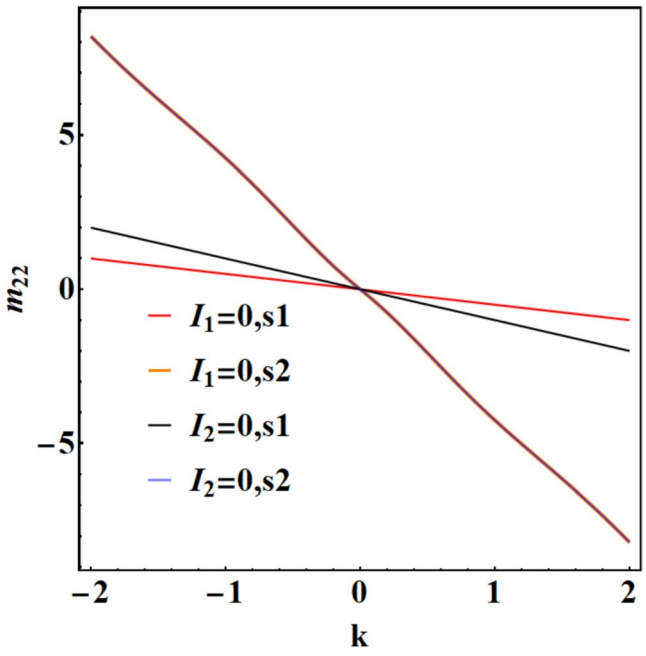

Fig. 13 For different values of k, the solutions of Eqs. (C.4) and (C.5), where S1 and S2 represent different solutions of an equation

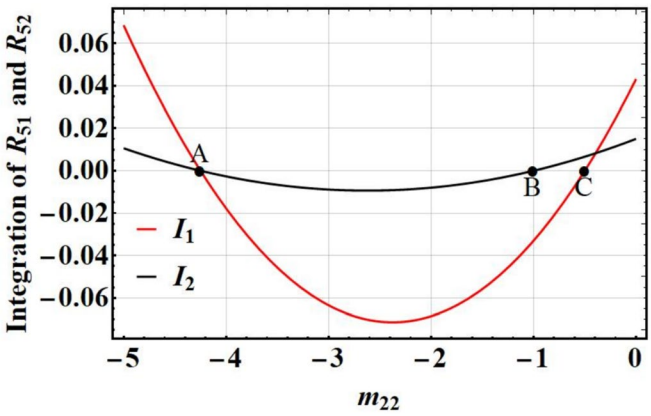

Fig. 14 The relationship between $I_i(i = 1, 2)$ and m_{22} when $k = 1$

$$\begin{aligned}
\left\langle x_{\mathrm{csr}}^2 \right\rangle_u &= k_{\mathrm{csr}}^2 \left(\int_{s_\mathrm{f}}^{s_0} \frac{R_{52}}{\sigma_z^{4/3}(s)} \mathrm{d}s \right)^2 \times I_\Gamma, \\
\left\langle x_{\mathrm{csr}}'^2 \right\rangle_u &= k_{\mathrm{csr}}^2 \left(\int_{s_\mathrm{f}}^{s_0} \frac{R_{51}}{\sigma_z^{4/3}(s)} \mathrm{d}s \right)^2 \times I_\Gamma, \\
\left\langle x_{\mathrm{css}} x_{\mathrm{csr}}' \right\rangle_u &= k_{\mathrm{csr}}^2 \left(\int_{s_\mathrm{f}}^{s_0} \frac{R_{52}}{\sigma_z^{4/3}(s)} \mathrm{d}s \right) \left(\int_{s_\mathrm{f}}^{s_0} \frac{R_{51}}{\sigma_z^{4/3}(s)} \mathrm{d}s \right) \times I_\Gamma.
\end{aligned} \tag{B.4}$$

where

$$I_\Gamma = \left(\int_{-\infty}^{+\infty} \lambda(u)\Gamma(u)\mathrm{d}u \right)^2 - \int_{-\infty}^{+\infty} \lambda(u)\Gamma^2(u)\mathrm{d}u. \tag{B.5}$$

Notice that these equations are held when only the linear transformation for z is considered. For the cases where $R_{56} \to 0$, the beam size σ_z remains constant along s. Then, the RMS of ss CSR kicks can be simplified as

$$\begin{aligned}
\left\langle x_{\mathrm{csr}}^2 \right\rangle_u &= I_{\mathrm{csr}} I_2^2, \\
\left\langle x_{\mathrm{csr}}'^2 \right\rangle_u &= I_{\mathrm{csr}} I_1^2, \\
\left\langle x_{\mathrm{css}} x_{\mathrm{csr}}' \right\rangle_u &= I_{\mathrm{csr}} I_1 I_2.
\end{aligned} \tag{B.6}$$

And

$$\begin{aligned}
I_i &= \int_{s_\mathrm{f}}^{s_0} R_{5i} \mathrm{d}s, \\
I_{\mathrm{csr}} &= \frac{k_{\mathrm{csr}}^2 I_\Gamma}{\sigma_z^{4/3}}.
\end{aligned} \tag{B.7}$$

C. Analytical solution for isochronous symmetric TBA cells with complete suppression of SS CSR effects

In this context, we exclusively consider a centrally symmetric TBA structure, where the side bend angles are identical, defined as $\theta_{\mathrm{B}_1} = \theta_{\mathrm{B}_3} = \theta_1$, and the angle of the middle bend is

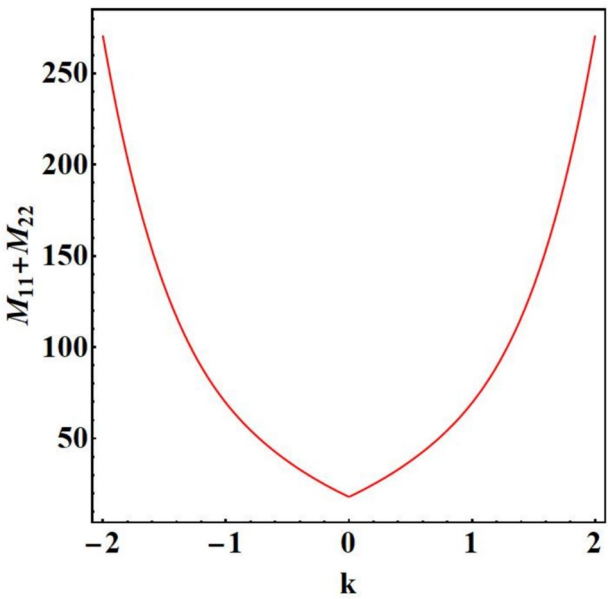

Fig. 15 The relationship between the transverse focusing parameter $\left|\hat{M}_{11} + \hat{M}_{22}\right|$ and k, where $k = 0$ is a singularity

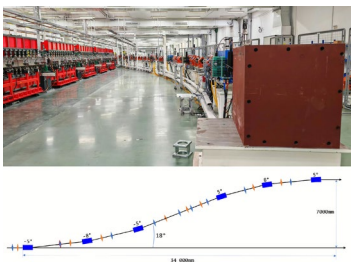

Fig. 16 (Color online) The experimental area (top) and layout (bottom) of LAD beamline. The diamonds represent quadrupole magnets, and the rectangles represent bending magnets

$\theta_{B_2} = k\theta_1$ ($k \subseteq [-2, 2]$). The strengths and positions of the quadrupole magnets exhibit symmetry about the midpoint, focusing solely on the interplay between the horizontal and longitudinal directions while disregarding the vertical direction and higher-order transfer matrices. Under the hard-edge model approximation, the transfer matrix for a bend with a small angle can be approximated as shown in Eq. (C.1). And the transfer matrix of the first matching section $\hat{M}_{q,1}$ between the bends is defined in Eq. (C.2). For the symmetric TBA cells, the second matching section meets $\hat{M}_{q,2} = \hat{M}_{q,1}^{-1}$, the superscript -1 denotes the reverse matrix.

$$\hat{M}_B = \begin{pmatrix} 1 & \rho\theta & 0 & \frac{\rho\theta^2}{2} \\ 0 & 1 & 0 & \theta \\ -\theta & -\frac{\rho\theta^2}{2} & 1 & -\frac{\rho\theta^3}{6} \\ 0 & 0 & 0 & 1 \end{pmatrix}. \tag{C.1}$$

$$\hat{M}_q = \begin{pmatrix} m_{11} & m_{12} & 0 & 0 \\ m_{21} & m_{22} & 0 & 0 \\ 0 & 0 & 1 & 0 \\ 0 & 0 & 0 & 1 \end{pmatrix}. \tag{C.2}$$

In the derivation, we assume that all bends have the same radius, denoted as ρ. When the structure satisfies the following conditions: (1) $R_{26,\mathrm{mid}} = 0$, (2) $R_{56,\mathrm{mid}} = 0$, (3) symmetric condition. To facilitate subsequent calculations, we eliminated m_{12} and m_{21}. The relation between the dimensionless quantities m_{11} and m_{22} can be expressed as:

$$\begin{aligned} m_{11} &= \frac{-16k + k^4 - 8m_{22} + 2k^3 m_{22}}{6k^2} \qquad (k > 0), \\ m_{11} &= -\frac{16k + k^4 + 8m_{22} + 2k^3 m_{22}}{6k^2} \qquad (k < 0). \end{aligned} \tag{C.3}$$

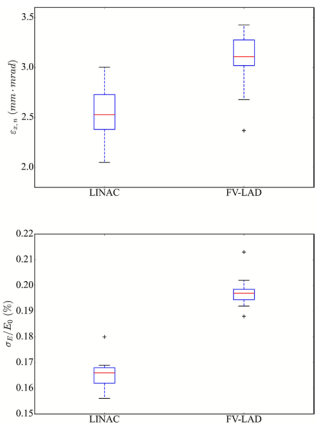

Fig. 17 The initial diagnostic results for the LAD beamline. The growth in horizontal emittance is approximately 22% (left), while the energy spread variation is about 18.6% (right)

Based on the relationships described in Eq. (C.3), the integrals for R_{51} and R_{52} in TBA cells can be expressed as follows:

$$\frac{36I_1k^2}{\theta_1^2\rho} = (k + 2m_{22})(28k + 12k^2 + 8k^4 + 3k^5 + 8m_{22} + 4k^3m_{22}) \quad (k \subseteq [-2, 2]), \tag{C.4}$$

$$\frac{36I_2k^2}{\theta_1^3\rho^2} = (k + m_{22})(28k + 12k^2 + 8k^4 + 3k^5 + 8m_{22} + 4k^3m_{22}) \quad (k \subseteq [-2, 2]). \tag{C.5}$$

To eliminate the influence of ss CSR completely, it is necessary to set I_1 and I_2 in Eq. (5) is equal to 0, which implies that the right-hand side of Eqs. (C.4) and (C.5) should be equal to 0. It is evident that for any given k, the relationship between m_{22} and k is shown in Fig. 13. As shown in the figure, for any angular ratio k, there exist four solutions (with the black and orange curves overlapping), which can make either I_1 or I_2 equal to zero. This overlapping indicates a solution that simultaneously satisfies both $I_1 = 0$ and $I_2 = 0$. When $k = 1$ (Fig. 14), the three solutions were $m_{22} = -\frac{17}{4}$ (point A), $m_{22} = -1$ (point B), $m_{22} = -\frac{1}{2}$ (point C). Points A and C are discussed in detail in Refs. [27] and [29]. According to these studies, both points can suppress the ss CSR effect, with point A (corresponding to the overlapping solution) completely eliminating the ss CSR effect. Furthermore, for any value of k, point A can be found such that both I_1 and I_2 are equal to zero. The relationship between m_{22} and k at this time is

$$\begin{aligned} m_{22} &= -\frac{28k + 12k^2 + 8k^4 + 3k^5}{4(2 + k^3)} \qquad (k \subseteq (0, 2]), \\ m_{22} &= \frac{28k - 12k^2 - 8k^4 + 3k^5}{4(-2 + k^3)} \qquad (k \subseteq [-2, 0)). \end{aligned} \tag{C.6}$$

Therefore, when m_{22} satisfies the conditions shown in Eq. (C.6), the TBA can achieve isochronicity while completely eliminating the impact of ss CSR. Simultaneously, it is essential to maintain the horizontal emittance of the bunch in order to connect multiple TBA cells and deflect the beam at a greater angle. This requires satisfying the criterion for periodic stable optics in the transverse direction, which is: $\left|\hat{M}_{11} + \hat{M}_{22}\right| \leq 2$, where $\hat{M}$ is the transfer matrix of the TBA cell.

$$\hat{M} = \hat{M}_{B_1}\hat{M}_q^{-1}\hat{M}_{B_2}\hat{M}_q\hat{M}_{B_1}. \tag{C.7}$$

By substituting the m_{22} obtained from Eq. (C.6) into Eq. (C.7), the transverse focusing parameter $\left|\hat{M}_{11} + \hat{M}_{22}\right|$ is determined, and it can be known that the relationship between this parameter and k is shown in Fig. 15. As k

approaches 0, the transverse focusing parameter reaches its minimum value of 17.25, yet it still fails to satisfy the condition for periodic stable optics. Additionally, due to the large transverse focusing parameter, controlling the transverse size of the bunch becomes challenging when connecting multiple cells in series. Thus, within the range $k \subseteq [-2, 2]$, there is no analytical solution that simultaneously satisfies the following: (1) Isochronicity. (2) Meeting optical stability conditions. (3) Complete elimination of the ss CSR effect. Therefore, it was necessary to obtain an asymptotic solution.

D. The large angle deflection beamline for SXFEL

Based on the $-I$ matrix method, a large-angle deflection (LAD) beamline has been designed. This project aims to study the CSR effects on bunches with high peak current. The beamline is implemented at the SXFEL, specifically at the exit of the main accelerating modules. The floor plan of the LAD is shown in Fig. 16. The total deflection angle of the LAD is $2 \times 18°$. Each TBA in the LAD consists of three bending magnets and four quadrupoles. Due to spatial limitations, the deflection angles of the two TBA cells are in opposite directions. To prevent interference between the LAD and adjacent beamlines, a 2 m drift section is introduced after the first bend, with the transverse dimension of the first quadrupole (marked with a red-edged diamond in Fig. 16) constrained to under 150 mm. The matching section contains seven quadrupoles, ensuring an I matrix for the transfer matrix between the entrances of the two TBA cells.

The quadrupole scan method was employed to measure the emittance at both the linac exit and the LAD exit. By scanning quadrupole strengths and measuring the transverse beam size on the screen, the emittance was obtained through curve fitting. The energy spread at both locations was measured using the spectrometer method. Using a dipole spectrometer, the beam spot was observed at the screen center. The central beam energy was determined from magnetic measurements, while the energy spread was calculated from the dispersed beam profile combined with the central energy parameters [39]. These initial beam diagnostics measurements were completed in June 2024, with preliminary results shown in Fig. 17. The normalized emittance at the exit of the main linac is 2.52 μm rad with an uncertainty of 0.27 μm rad, and the normalized emittance at the exit of LAD beamline is 3.0 μm rad with an uncertainty of 0.27 μm rad, showing a relative increase of approximately 22%. The energy spread at the exit of main-linac is 0.166% with an uncertainty of 0.0058%, and the energy spread at the exit of LAD beamline is 0.2% with an uncertainty of 0.0043%, corresponding to a variation of 18.6%. Further experimental investigations are ongoing, and the results will be presented in forthcoming publications.

Declarations

Conflict of interest Hai-Xiao Deng is an editorial board member for Nuclear Science and Techniques and was not involved in the editorial review, or the decision to publish this article. All authors declare that there are no conflict of interest.

References

1. Z. Zhao, D. Wang, Q. Gu et al., Status of the SXFEL facility. Appl. Sci. **7**, 607 (2017). https://doi.org/10.3390/app7060607
2. A. Bartnik, N. Banerjee, D. Burke et al., CBETA: first multipass superconducting linear accelerator with energy recovery. Phys. Rev. Lett. **125**, 044803 (2020). https://doi.org/10.1103/PhysRevLett.125.044803
3. S. Di Mitri, M. Cornacchia, B. Diviacco et al., Bridging the gap of storage ring light sources and linac-driven free-electron lasers. Phys. Rev. Accel. Beams **24**, 060702 (2021). https://doi.org/10.1103/PhysRevAccelBeams.24.060702
4. P.H. Williams, D. Angal-Kalinin, D.J. Dunning et al., Recirculating linac free-electron laser driver. Phys. Rev. ST Accel. Beams **14**, 050704 (2011). https://doi.org/10.1103/PhysRevSTAB.14.050704
5. Z.T. Zhao, Z. Wang, C. Feng et al., Energy recovery linac based fully coherent light source. Sci. Rep. **11**, 23875 (2021). https://doi.org/10.1038/s41598-021-03354-0
6. Z. Zhu, D. Gu, J. Yan et al., Inhibition of current-spike formation based on longitudinal phase space manipulation for high-repetition-rate X-ray FEL. Nucl. Instrum. Methods Phys. Res. Sect. A **1026**, 166172 (2022). https://doi.org/10.3390/app7060607
7. N. Nakamura, R. Kato, H. Sakai et al., High-power EUV free-electron laser for future lithography. Jpn. J. Appl. Phys **62**, SG0809 (2023). https://doi.org/10.35848/1347-4065/acc18c
8. T. Nakazato, M. Oyamada, N. Niimura et al., Observation of coherent synchrotron radiation. Phys. Rev. Lett. **63**, 1245 (1989). https://doi.org/10.1103/PhysRevLett.63.1245
9. C. Behrens, Detection and spectral measurements of coherent synchrotron radiation at FLASH (2010). ISSN 1435-8085; TRN: DE10F2606
10. Y. Jing, Y. Hao, V.N. Litvinenko, Compensating effect of the coherent synchrotron radiation in bunch compressors. Phys. Rev. ST Accel. Beams **16**, 060704 (2013). https://doi.org/10.1103/PhysRevSTAB.16.060704
11. S. Di Mitri, M. Cornacchia, S. Spampinati, Cancellation of coherent synchrotron radiation kicks with optics balance. Phys. Rev. Lett. **110**, 014801 (2013). https://doi.org/10.1103/PhysRevLett.110.014801
12. D. Douglas, S. Benson, R. Li et al., Control of synchrotron radiation effects during recirculation with bunch compression. Thomas Jefferson National Accelerator Facility (TJNAF), Newport News, VA (2015). OSTI ID: 1178577
13. J.A.G. Akkermans, S. Di Mitri, D. Douglas et al., Compact compressive arc and beam switchyard for energy recovery linac-driven ultraviolet free electron lasers. Phys. Rev. Accel. Beams **20**, 080705 (2017). https://doi.org/10.1103/PhysRevAccelBeams.20.080705
14. D.Z. Khan, T.O. Raubenheimer, Novel bunch compressor chicane: the five-bend chicane. Phys. Rev. Accel. Beams **25**, 090701 (2022). https://doi.org/10.1103/PhysRevAccelBeams.25.090701
15. S. Di Mitri, Feasibility study of a periodic arc compressor in the presence of coherent synchrotron radiation. Nucl. Instrum. Methods Phys. Res. Sect. A **806**, 184–192 (2016). https://doi.org/10.1016/j.nima.2015.10.015

16. X.Y. Huang, X. Cui, S. Gu et al., Feasibility analysis of emittance preservation during bunch compression in the presence of coherent synchrotron radiation in an arc, in *8th International Particle Accelerator Conference (IPAC'17)*, Copenhagen, Denmark, 14–19 May, 2017. JACOW, Geneva, Switzerland (2017). https://doi.org/10.18429/JACoW-IPAC2017-THPAB026
17. C.Y. Zhang, Y. Jiao, W.H. Liu et al., Suppression of the coherent synchrotron radiation induced emittance growth in a double-bend achromat with bunch compression. Phys. Rev. Accel. Beams **26**, 050701 (2023). https://doi.org/10.1103/PhysRevAccelBeams.26.050701
18. S. Heifets, G. Stupakov, Beam instability and microbunching due to coherent synchrotron radiation. PACS2001, in *Proceedings of the 2001 Particle Accelerator Conference (Cat. No.01CH37268)*, Chicago, IL, USA, 2001, pp. 1856–1858. https://doi.org/10.1109/PAC.2001.987206
19. C.Y. Tsai, S. Di Mitri, D. Douglas et al., Conditions for coherent-synchrotron-radiation-induced microbunching suppression in multibend beam transport or recirculation arcs. Phys. Rev. Accel. Beams **20**, 024401 (2017). https://doi.org/10.1103/PhysRevAccelBeams.20.024401
20. C.Y. Tsai, An alternative view of coherent synchrotron radiation induced microbunching development in multibend recirculation arcs. Nucl. Instrum. Methods Phys. Res. Sect. A **943**, 162499 (2019). https://doi.org/10.1016/j.nima.2019.162499
21. R. Hajima, A first-order matrix approach to the analysis of electron beam emittance growth caused by coherent synchrotron radiation. Jpn. J. Appl. Phys. **42**, L974 (2003). https://doi.org/10.1143/JJAP.42.L974
22. R. Hajima, An analysis of the coherent synchrotron radiation effect in an energy-recovery linac by first-order transfer matrix, in *the 14th Symposium on Accelerator Science and Technology*, Tsukuba, Japan, November 2003
23. Y. Jiao, X.H. Cui, X.Y. Huang et al., Generic conditions for suppressing the coherent synchrotron radiation induced emittance growth in a two-dipole achromat. Phys. Rev. ST Accel. Beams **17**, 060701 (2014). https://doi.org/10.1103/PhysRevSTAB.17.060701
24. X.Y. Huang, X. Cui, Y. Jiao et al., Minmization of the emittance growth induced by coherent synchrotron radiation in arc compressor, in *Proceedings of the 37th International Free Electron Laser Conference (FEL 2015),* Daejeon, Korea, JACoW (2015). ISBN 978-3-95450-134-2
25. X.Y. Huang, Y. Jiao, G. Xu et al., Suppression of the emittance growth induced by coherent synchrotron radiation in triple-bend achromats. Chin. Phys. C **39**, 057001 (2015). https://doi.org/10.1088/1674-1137/39/5/057001
26. X.H. Cui, Y. Jiao, X.Y. Huang et al., Suppression of the CSR emittance in a single achromatic cell, in *Proceedings of 12th Symposium on Accelerator Physics (SAP 2014)*, Lanzhou, China, 13–15 August, 2014
27. C.Y. Zhang, Y. Jiao, C.-Y. Tsai, Quasi-isochronous triple-bend achromat with periodic stable optics and negligible coherent-synchrotron-radiation effects. Phys. Rev. Accel. Beams **24**, 060701 (2021). https://doi.org/10.1103/PhysRevAccelBeams.24.060701
28. C.Y. Zhang, Y. Jiao, C.Y. Tsai, Optimization of a TBA with stable optics and minimal longitudinal dispersion and CSR-induced emittance growth, in *12th International Particle Accelerator Conference (IPAC'21),* Campinas, SP, Brazil, 24–28 May, 2021. JACOW Publishing, Geneva, Switzerland (2021). https://doi.org/10.18429/JACoW-IPAC2021-MOPAB056
29. M. Venturini, Design of a triple-bend isochronous achromat with minimum coherent-synchrotron-radiation-induced emittance growth. Phys. Rev. Accel. Beams **19**, 064401 (2016). https://doi.org/10.1103/PhysRevAccelBeams.19.064401
30. P. Emma, R. Brinkmann, Emittance dilution through coherent energy spread generation in bending systems, in *Proceedings of the 1997 Particle Accelerator Conference (Cat. No. 97CH36167)*. Vancouver, BC, Canada, 1997, pp. 1679–1681. https://doi.org/10.1109/PAC.1997.750799
31. K. Deb, J. Sundar, Reference point based multi-objective optimization using evolutionary algorithms, in *Proceedings of the 8th Annual Conference on Genetic and Evolutionary Computation* (2006). https://doi.org/10.1145/1143997.1144112
32. D. Sagan, Bmad: a relativistic charged particle simulation library. Nucl. Instrum. Methods Phys. Res. Sect. A **558**, 356–359 (2006). https://doi.org/10.1016/j.nima.2005.11.001
33. M. Borland, Elegant: a flexible SDDS-compliant code for accelerator simulation, in *6th International Computational Accelerator Physics Conference (ICAP 2000),* Darmstadt, Germany, 11–14 September, 2000, LS-287. https://doi.org/10.2172/761286
34. Z.T. Zhao, D. Wang, L.X. Yin et al., Shanghai soft X-ray free electron laser test facility. Acta Opt. Sin. **41**, 0114006 (2021). https://doi.org/10.3788/AOS202141.0114006
35. B. Liu, C. Feng, D. Gu et al., The SXFEL upgrade: from test facility to user facility. Appl. Sci. **12**, 176 (2021). https://doi.org/10.3390/app12010176
36. X.J. Chen, S. Chen, D. Wang, Suppression of coherent synchrotron radiation-induced emittance growth in a multi-bend deflection line (2024). arXiv:2405.05585
37. G. Stupakov, P. Emma, CSR wake for a short magnet in ultrarelativistic limit. Particle accelerator, in *Proceedings of 8th European Conference, EPAC 2002,* Paris, France, 3–7 June, 2002, pp. 1479–1481.
38. E.L. Saldin, E.A. Schneidmiller, M.V. Yurkov, On the coherent radiation of an electron bunch moving in an arc of a circle. Nucl. Instrum. Methods Phys. Res. Sect. A **398**, 373–394 (1997). https://doi.org/10.1016/S0168-9002(97)00822-X
39. M.G. Minty, F. Zimmermann, *Measurement and Control of Charged Particle Beams* (Springer Nature, Berlin, 2003). https://doi.org/10.1007/978-3-662-08581-3